

## Article

# Martensitic Transformation and Barocaloric Effect in Co-V-Ga-Fe Paramagnetic Heusler Alloy

Jie Liu <sup>1,2</sup>, Zhe Li <sup>2,\*</sup> , Hongwei Liu <sup>2,3</sup>, Litao Yu <sup>1,2</sup>, Yuanlei Zhang <sup>2</sup>, Yiming Cao <sup>2</sup>, Kun Xu <sup>2</sup> and Yongsheng Liu <sup>1,\*</sup>

<sup>1</sup> Department of Physics, Shanghai University of Electric Power, Shanghai 200090, China; liujie0612@126.com (J.L.); yltgyj@163.com (L.Y.)

<sup>2</sup> Center for Magnetic Materials and Devices, College of Physics and Electronic Engineering, Qujing Normal University, Qujing 655011, China; yuanleizhang@mail.qjnu.edu.cn (Y.Z.); ymcao@mail.qjnu.edu.cn (Y.C.); xukun@mail.qjnu.edu.cn (K.X.)

<sup>3</sup> Key Laboratory for Anisotropy and Texture of Materials (Ministry of Education), School of Material Science and Engineering, Northeastern University, Shenyang 110819, China; vig3147@163.com

\* Correspondence: zheli@mail.qjnu.edu.cn (Z.L.); ysliu@shiep.edu.cn (Y.L.)

**Abstract:** In the present study, polycrystalline  $\text{Co}_{50}\text{V}_{34}\text{Ga}_{16-x}\text{Fe}_x$  ( $1 \leq x \leq 2$ ) quaternary Heusler alloys were fabricated by the arc-melting method. It was found that they undergo a paramagnetic martensitic transformation (MT) from the  $L2_1$ -type cubic austenitic structure to the  $D0_{22}$  tetragonal martensitic structure. With the increase of the Fe concentration, the MT shifts towards a higher temperature range, which is strongly related to the variation of the valence electron concentration. Moreover, it was also found that the MT exhibited by every alloy is sensitive to the applied hydrostatic pressure due to a relatively high difference in volume between the two phases. By using the quasi-direct method based on caloric measurements, the barocaloric effect (BCE) associated with the hydrostatic pressure-driven MT was estimated in the studied alloys. The results demonstrated that the sample with  $x = 1.5$  performs an optimal BCE among these three alloys.

**Keywords:** Heusler alloy; martensitic transformation; barocaloric effect



**Citation:** Liu, J.; Li, Z.; Liu, H.; Yu, L.; Zhang, Y.; Cao, Y.; Xu, K.; Liu, Y. Martensitic Transformation and Barocaloric Effect in Co-V-Ga-Fe Paramagnetic Heusler Alloy. *Metals* **2022**, *12*, 516. <https://doi.org/10.3390/met12030516>

Academic Editors: Ryosuke Kainuma and João Pedro Oliveira

Received: 27 January 2022

Accepted: 15 March 2022

Published: 17 March 2022

**Publisher's Note:** MDPI stays neutral with regard to jurisdictional claims in published maps and institutional affiliations.



**Copyright:** © 2022 by the authors. Licensee MDPI, Basel, Switzerland. This article is an open access article distributed under the terms and conditions of the Creative Commons Attribution (CC BY) license (<https://creativecommons.org/licenses/by/4.0/>).

## 1. Introduction

Currently, solid-state refrigeration, based on the caloric effect produced by a solid-state substance, is expected to replace the conventional gas compression and expansion technique in consideration of energy efficiency and the environment. In general, solid-state materials with large caloric effects are those that usually exhibit first-order structural transformation (FOST) induced by various external stimuli, such as the magnetic field, electric field, uniaxial stress, and hydrostatic pressure [1]. Among them, the caloric effect of materials induced by the applied hydrostatic pressure is broadly referred to as the barocaloric effect, which has received much attention for the last decade, because such a refrigerating mode is readily approachable by present technologies [2]. Until now, the BCE has been developed in a lot of solid-state materials, such as Ni-Mn-based Heusler alloys [3–7], the itinerant-electron system [8–10], antiferromagnetic compounds [11], hexagonal  $\text{Ni}_2\text{In}$ -type compounds [12–14], piezoelectric ceramics [15,16], the superionic conductor [17], the organic–inorganic hybrid perovskite [18], plastic crystals [19,20], and so on.

As is well known, the stoichiometric,  $\text{Co}_2\text{VGa}$ , with a full Heusler structure, is a half-metallic ferromagnetism (HEM) material, and some theoretical and experimental works have been devoted to studying the spin polarization, Curie temperature, and magnetic moment in this alloy, due to its potential application in spin injection devices [21,22]. In

recent years, the first-order martensitic transformation (MT) without a change of magnetic order has been also found in a series of non-stoichiometric Co-V-Ga ternary alloys [23]. After that, a low temperature metamagnetic martensitic transformation was successively developed in  $\text{Co}_{50}\text{V}_{34}\text{Ga}_{16}$  [24] and  $\text{Co}_{46}\text{Fe}_5\text{V}_{34}\text{Ga}_{15}$  [25]. In addition, a considerable BCE produced by the hydrostatic pressure-driven MT was respectively reported in  $\text{Co}_{51}\text{Fe}_1\text{V}_{33}\text{Ga}_{15}$  [26] and  $\text{Co}_{50}\text{V}_{31.5}\text{Fe}_{2.5}\text{Ga}_{16}$  alloys [27], which can be ascribed to the fact that the introduction of Fe can enlarge the difference in volume between austenitic and martensitic phases and bring about a large lattice entropy change. In the present study, we used a small quantity of Fe atoms as a chemical substitution for Ga atoms and synthesized the  $\text{Co}_{50}\text{V}_{34}\text{Ga}_{16-x}\text{Fe}_x$  ( $1 \leq x \leq 2$ ) quaternary alloys with nominal composition. The experimental results demonstrated that the studied alloys exhibit a paramagnetic MT, which is accompanied by an obvious volume change, thus giving rise to a relatively high transition entropy change. Because of this, a large BCE was obtained in these alloys under an applied low hydrostatic pressure.

## 2. Experimental Method

The  $\text{Co}_{50}\text{V}_{34}\text{Ga}_{16-x}\text{Fe}_x$  ( $x = 1, 1.5$  and  $2$ ) alloys with nominal compositions were fabricated by using a traditional arc-melting approach under a high-purity argon atmosphere with a pressure of  $10^{-1}$  Pa. All of these samples were remelted four times to ensure their homogeneity, and the weight loss after melting was less than 0.2% for every sample. The obtained ingots were annealed at 1473 K for 1 day in a high-vacuum quartz tube followed by quenching into ice water. The actual composition of the prepared alloys was determined by the energy-dispersive spectrometer (EDS, ProX, Phenom) corresponding to  $\text{Co}_{49.81}\text{V}_{34.11}\text{Ga}_{14.94}\text{Fe}_{1.13}$ ,  $\text{Co}_{49.94}\text{V}_{34.06}\text{Ga}_{14.54}\text{Fe}_{1.46}$ , and  $\text{Co}_{49.66}\text{V}_{34.27}\text{Ga}_{13.96}\text{Fe}_{2.12}$ , respectively. The microstructure of the specimen was taken by the scanning electron microscope (ProX, Phenom). The crystal structure of these alloys was identified by utilizing the powder X-ray diffraction (XRD) technique (Ultima-IV, Rigaku Inc., Tokyo, Japan), and the FullProf program was used for the Rietveld structure refinement of the powder XRD spectrum [28]. The magnetization measurements were performed on a vibrating sample magnetometer (VSM, Versalab, Quantum Design Inc., San Diego, CA, USA). Heat flow data at different hydrostatic pressures were collected from the commercial differential scanning calorimeter, which is equipped with a high-pressure nitrogen generator ( $\mu\text{DSC7 EVO}$ , Setaram Inc., Caluire, France), and the scanning rate of temperature is 1 K/min. The temperature dependence of the spontaneous strain was measured by standard strain-gauge technique using a piece of the rectangular specimen with dimensions of  $1 \times 2 \times 3 \text{ mm}^3$ .

## 3. Results and Discussion

Figure 1a–c gives the XRD patterns of  $\text{Co}_{50}\text{V}_{34}\text{Ga}_{16-x}\text{Fe}_x$  at room temperature. As shown in this figure, it can be found that the samples with  $x = 1$  and  $x = 1.5$  possess an  $L2_1$ -type cubic austenitic structure, and their lattice parameters are calculated to be 5.7593 Å and 5.7837 Å, respectively. The increase of lattice parameters could be explained by the fact that the atom radius of Fe is larger than that of Ga, which also leads to the fact that the cell volume of the austenitic phase increases from 191.03 Å<sup>3</sup> to 193.47 Å<sup>3</sup>. With the further increase of Fe content, it can be clearly observed that the sample with  $x = 2$  exhibits a  $D0_{22}$  tetragonal martensitic structure with the lattice parameters of  $a = 3.8457$  Å and  $c = 6.5389$  Å, which means that its structure transformation happens above room temperature. The microstructure of the sample with  $x = 1.5$  is shown in Figure 1d. From the SEM micrograph, it can be observed that the matrix shows a typical austenitic morphology, and no precipitates can be found on the grain boundaries. This means that there is no microscale phase separation in this sample. To analyze the occupied sites for the different atoms in the lattice of the austenitic phase, the  $L2_1$ -type Heusler structure, consisting of four interpenetrating fcc sublattices, is constructed in Figure 1d. From this figure, it is obvious that the four equivalent atomic sites are enclosed in the unit cell, which successively denotes as A, B, C, and D positions along the diagonal body. According

to the early hyperfine field studies of site occupation in Heusler alloys [29,30], the main group of elements usually occupies the D site of the Heusler structure. However, for the transition metals, the preferential choice of atomic site occupancy in this structure is strongly dependent on the number of valence electrons in them, i.e., the transition metals with higher valence electrons that prefer to occupy A and C sites, while those of the lower valence electrons tend to occupy the B site. Based on the aforementioned rules of atomic occupancy, for the studied alloys, the Co atoms should occupy A and C sites, whereas the introduced Fe atoms should replace a small number of V atoms and occupy the B site due to the higher valence electrons. Moreover, the extra V and all Ga atoms should occupy the D site to form a highly ordered parent structure. These analyses also suggest that the substitution in the chemical composition is not necessarily equivalent to the substitution in the atomic site.

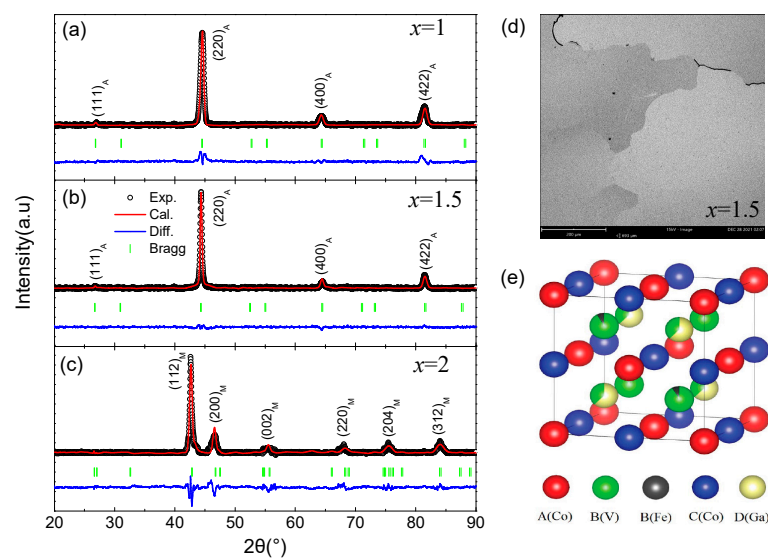


**Figure 1.** (a–c) The X-ray diffraction patterns of  $\text{Co}_{50}\text{V}_{34}\text{Ga}_{16-x}\text{Fe}_x$  alloys at room temperature. (d) The micrograph taken by SEM for the sample with  $x = 1.5$ . (e) The  $L2_1$ -type Heusler structure, which consists of four interpenetrating fcc sublattices.

The temperature dependence of magnetization  $M(T)$  of  $\text{Co}_{50}\text{V}_{34}\text{Ga}_{16-x}\text{Fe}_x$  are presented in Figure 2a, which were measured under a magnetic field of 500 Oe. From these  $M(T)$  curves, we can find that the studied alloys exhibit a very low magnetization, implying that they locate in a weak-magnetic state within the measured temperature range. For every sample, an abrupt drop of magnetization starts to occur at  $M_s$  and then gradually holds steady at  $M_f$  during cooling. This behavior corresponds to the exothermic peak measured in DSC data (see Figure 2b), indicating the occurrence of forward MT. Both  $M_s$  and  $M_f$  are denoted as forward martensite starting and finishing temperatures, respectively. During heating, an abrupt jump of magnetization starts to happen at  $A_s$  and then gradually remains unchanged at  $A_f$ , which is reflected in the endothermic peak measured in DSC data (see Figure 2b), indicating the occurrence of reverse MT. Both  $A_s$  and  $A_f$  are denoted as reverse martensite starting and finishing temperatures, respectively. Between heating and cooling, a conspicuous thermal hysteresis ( $\Delta T$ ) can be distinguished, which suggests that the MT exhibited by these alloys is characterized by the FOMT. However, it is worth noting that the  $\Delta T$  exhibited by the studied alloys is significantly lower than that observed in other Co-V-Ga-based Heusler alloys [23,24,26,27], which can be ascribed to the decrease of precipitates. Table 1 lists the valence electron concentration ( $e/a$ ), characteristic temperatures, and thermal hysteresis of the MT for the studied alloys. It is apparent that the increase of  $e/a$  shifts the MT towards a higher temperature range. This suggests that the  $e/a$  plays a dominant role to stabilize the cubic austenitic structure. The same behavior was also reported in  $\text{Co}_{51-y}\text{Fe}_y\text{V}_{34}\text{Ga}_{15}$  and  $\text{Co}_{52}\text{V}_{29-x}\text{Ga}_{19-x}$  alloys [25,31]. In addition, the

magnetic properties at different phases for the studied alloys are further analyzed by the isothermal magnetization curves, measured at 340 K and 260 K, as shown in Figure 2c–e. From these figures, the isothermal curves measured at 340 K almost presents a linear behavior without magnetic hysteresis in magnetization and demagnetization procedures, which states that all samples have a typically paramagnetic character at their austenitic phase. However, an inconspicuous curvature can be detected in the initial magnetization stage of the studied alloys. Such a behavior is in accordance with that observed in the  $\text{Co}_{50}\text{V}_{34}\text{Ga}_{16}$  alloy synthesized by a directional solidification technique and can be understood by the existence of the Griffiths phase [32]. In the case of the martensitic phase, it is obvious that the isothermal curve for each sample displays a nonlinear behavior at a low field range and still resumes a linearly variation with an increasing magnetic field. The former behavior can be ascribed to the enhancement of magnetocrystalline anisotropy caused by the change of crystal symmetry. Considering that the magnetization of martensite keeps the same order of magnitude when compared with that of the austenite, we can figure out that the variation of structure is not accompanied by the change of spin order, i.e., the MT exhibited by the studied alloys should take place in the paramagnetic state.

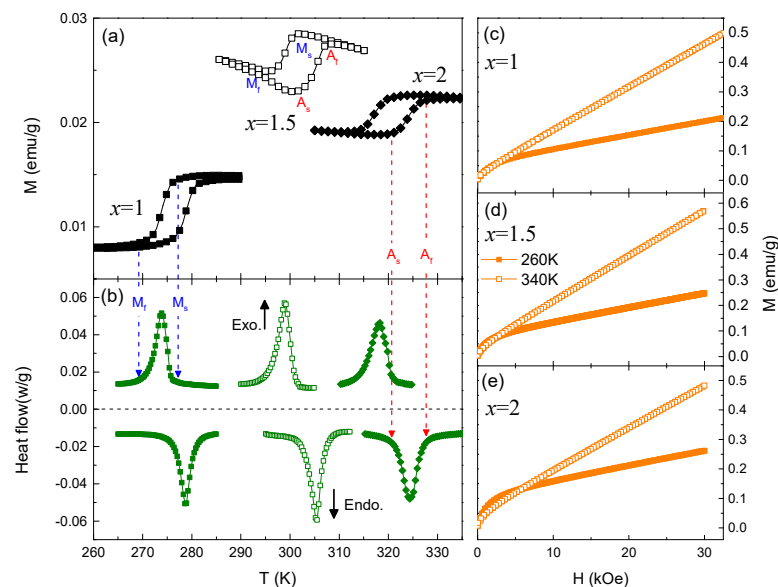


**Figure 2.** (a) The temperature dependence of the magnetization for  $\text{Co}_{50}\text{V}_{34}\text{Ga}_{16-x}\text{Fe}_x$  alloys at a magnetic field of 500 Oe. (b) The heat flow curves for these alloys measured in the transforming range with continuous cooling and heating. (c–e) The isothermal magnetization curves measured respectively at 260 K and 340 K for these alloys.

**Table 1.** The valence electron concentration ( $e/a$ ), characteristic temperatures ( $M_s$ ,  $M_f$ ,  $A_s$ , and  $A_f$ ) of MT, thermal hysteresis ( $\Delta T$ ), and equilibrium temperatures ( $T_0$  and  $T'_0$ ) of direct and reverse MTs for  $\text{Co}_{50}\text{V}_{34}\text{Ga}_{16-x}\text{Fe}_x$  alloys.

$x$	$e/a$	$M_s$ (K)	$M_f$ (K)	$A_s$ (K)	$A_f$ (K)	$\Delta T$ (K)	$T_0$ (K)	$T'_0$ (K)
1	6.73	276	269	275	282	6	274	279
1.5	6.755	302	295	301	309	6.5	299	306
2	6.78	321	313	319	328	6.5	318	324

To study the effect of the hydrostatic pressure on MT for  $\text{Co}_{50}\text{V}_{34}\text{Ga}_{16-x}\text{Fe}_x$ , the DSC curves were measured under applied different hydrostatic pressures, as described in Figure 3a–c. As the hydrostatic pressure increases from 0 to 0.8 kbar, it can be found that the two well-defined peaks induced by direct and reverse MTs move to high temperatures simultaneously. This is a consequence of the fact that the hydrostatic pressure tends to stabilize martensitic structure, which owns a relatively lower volume when compared

with the austenitic structure. Figure 3d–f further shows the equilibrium temperatures of MT change with the applied hydrostatic pressure. Both  $T_0$  and  $T'_0$  signify the equilibrium temperature at forward and reverse MTs, which are derived from the peak values of exothermic and endothermic curves (their numerical values are also listed in Table 1). As observed in these figures, a monotonic relationship between the equilibrium temperatures and the hydrostatic pressure is observed in every alloy. By linear fitting (see red solid line), the migration rates of  $T_0$ , with respect to the hydrostatic pressure ( $dT_0/dp$ ), are equal to  $\sim 2.74$  K/kbar for  $x = 1$ ,  $\sim 2.56$  K/kbar for  $x = 1.5$ , and  $\sim 2.39$  K/kbar for  $x = 2$ . These values can be comparable to those previously reported in many barocaloric alloys [2]. As compared to  $dT_0/dp$ , it can be explored that the values of  $dT'_0/dp$  for all alloys slightly decrease. Similar behavior was also observed in Ni-Mn-based Heusler alloys, which originates from the difference of latent heat during forward and reverse MTs [33].

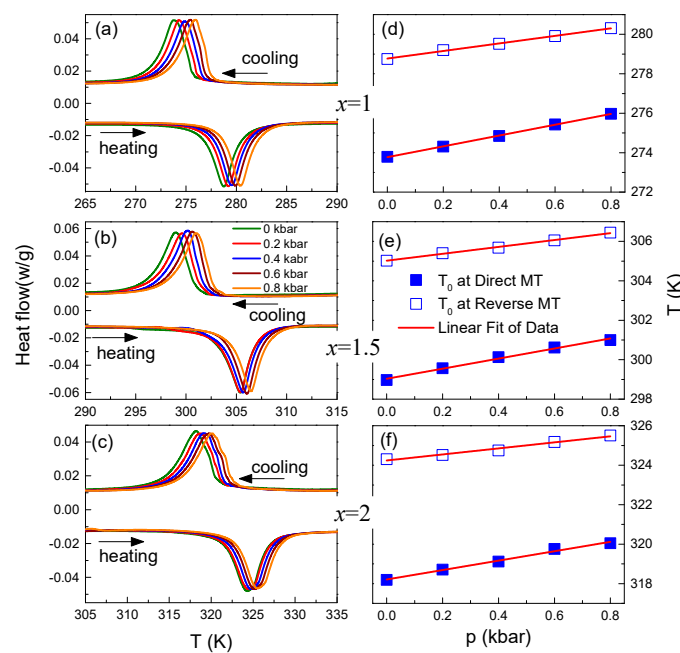


**Figure 3.** (a–c) The heat flow curves measured at applied hydrostatic pressure in the range of 0 to 0.8 kbar for  $\text{Co}_{50}\text{V}_{34}\text{Ga}_{16-x}\text{Fe}_x$  alloys. (d–f) The applied hydrostatic pressure dependence of equilibrium temperatures at forward ( $T_0$ ) and reverse ( $T'_0$ ) MTs for these alloys; the red solid line is their best linear fit.

In terms of the heat flow data, the relative entropy in the transforming range,  $S'(T, p) = S(T, p) - S(T_{ref}, p)$ , is deduced from the simultaneous integral equations, as put forward in Ref. [2], assuming the heat capacity to be independent of the pressure outside the transforming range. Such an assumption is based on the fact that the introduction of a low hydrostatic pressure has a trivial impact on the thermal expansion effect of the studied alloys outside the transforming range [31]. Here, the  $T_{ref}$  represents the reference temperature, which is close to the value of  $M_f$  for the studied alloys. By following this method, the  $S'(T, p)$  curves of  $\text{Co}_{50}\text{V}_{34}\text{Ga}_{16-x}\text{Fe}_x$  across the forward MT are recorded in Figure 4a–c. From the curves plotted at ambient pressure, the value of transition entropy change ( $\Delta S_{tr}$ ) is determined to be 26 J/kg K for  $x = 1$ , 30 J/kg K for  $x = 1.5$ , and 27 J/kg K for  $x = 2$ . These values can compete with lots of famous magnetocaloric materials showing a FOMT [34–36]. In addition, it is worth noting that the effect of the low hydrostatic pressure on the values of  $\Delta S_{tr}$  is negligible. Figure 4d–f illustrates the spontaneous strain as a function of temperature for  $\text{Co}_{50}\text{V}_{34}\text{Ga}_{16-x}\text{Fe}_x$  measured in a cooling–heating cycle. Accompanied by the occurrence of forward and reverse MT, all alloys perform a reproducible spontaneous transition strain induced by temperature, which means that there exists an obvious volume difference between their austenitic and martensitic phases. The changes of

molar volume ( $\Delta V = V_A - V_M$ , both  $V_A$  and  $V_M$  represent the molar volume of austenite and martensite, respectively) upon MT at an ambient pressure for the studied alloys can be examined by using the Clausius–Clapeyron (C–C) equation:  $\Delta V = \Delta S_{tr} \Delta(dT_0/dp)$ . From this formula, the values of  $\Delta V$  for the studied alloy are calculated to be  $\sim 0.041 \text{ cm}^3/\text{mol}$  for  $x = 1$ ,  $\sim 0.044 \text{ cm}^3/\text{mol}$  for  $x = 1.5$ , and  $\sim 0.037 \text{ cm}^3/\text{mol}$  for  $x = 2$ . Combining the molar volume of the austenite or martensite (calculated using the lattice parameters of the XRD results), the resultant relative volume changes ( $\epsilon$ ) between the two phases are equal to  $\sim 0.57\%$  for  $x = 1$ ,  $\sim 0.61\%$  for  $x = 1.5$ , and  $\sim 0.51\%$  for  $x = 2$ . These values are significantly larger than some Ni-Mn-based ferromagnetic Heusler alloys [3–5] and most ferroelectric compounds [15,16]. Because the magnitude of latent heat mainly stems from the contribution of the volume change in crystallography, the sample with  $x = 1.5$  performs the optimal barocaloric parameters (i.e.,  $\Delta S_{tr}$  and  $\Delta T_{ad}^{id}$ ) among these three alloys. Such experimental findings also indicate that a large BCE induced by the applied hydrostatic pressure can be anticipated in the studied alloys.

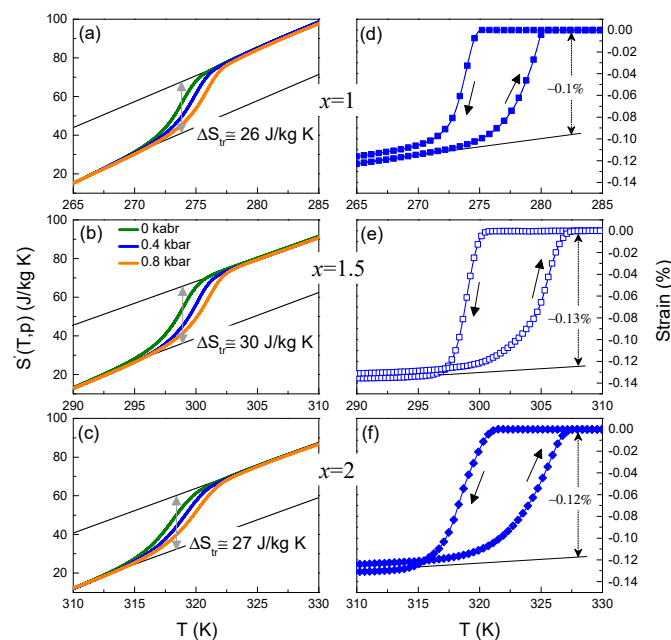


**Figure 4.** (a–c) The relative entropy as function of temperature across the forward transforming range under selected hydrostatic pressures for  $\text{Co}_{50}\text{V}_{34}\text{Ga}_{16-x}\text{Fe}_x$  alloys; the vertical double arrow represents the transition entropy change ( $\Delta S_{tr}$ ). (d–f) The spontaneous strain of these alloys measured in the process of forward and reverse MTs.

To confirm this point, as mentioned above, the temperature dependence of isothermal entropy change ( $\Delta S_T$ ) during the forward MT of  $\text{Co}_{50}\text{V}_{34}\text{Ga}_{16-x}\text{Fe}_x$  alloys, for the hydrostatic pressure change of 0.4 kbar and 0.8 kbar, is depicted in Figure 5a–c. Here, the value of  $\Delta S_T$  was calculated from the  $S'(T, p)$  curves (see Figure 4a–c) by using the formula:  $\Delta S_T(T, \Delta p) = S'(T, p) - S'(T, p = 0)$ . As evidenced from Figure 5a–c, a sharp peak can be observed around the  $T_0$  for the studied alloys, and its height and width are developed with the increase of the applied hydrostatic pressure. These experimental observations prove the substantive characteristics of BCE associated with the hydrostatic pressure-driven MT. The maximum  $\Delta S_T$  at  $\Delta p = 0.8 \text{ kbar}$  reaches  $\sim 15 \text{ J/kg K}$  for  $x = 1$ ,  $\sim 17 \text{ J/kg K}$  for  $x = 1.5$ , and  $\sim 11 \text{ J/kg K}$  for  $x = 2$ . Moreover, the value of  $\Delta T_{ad}$  can also be obtained from the  $S'(T, p)$  curves (see Figure 4a–c) by employing the formula:  $\Delta T_{ad}(T, \Delta p) = T(S', p) - T(S', p = 0)$ . Figure 5d,e shows the  $\Delta T_{ad}$  as a function of temperature under the same pressure changes. For all alloys, the evolution of  $\Delta T_{ad}$  with the temperature at different  $\Delta p$  demonstrates a similar behavior as those observed in the  $\Delta S_T(T)$  curves. The maximum  $\Delta T_{ad}$  at  $\Delta p = 0.8 \text{ kbar}$  is estimated to be  $\sim 1.6 \text{ K}$  for  $x = 1$ ,

$\sim 1.65$  K for  $x = 1.5$ , and  $\sim 1.5$  K for  $x = 2$ . Apparently, the maximum  $\Delta S_T$  obtained in these alloys at  $\Delta p = 0.8$  kbar is completely irreversible and significantly lower than the values of their  $\Delta S_{tr}$ . This is because of the insufficient application of hydrostatic pressure, which can only transform a part of the austenite to the martensite but cannot overcome the thermal hysteresis during MT. As a matter of fact, the critical applied hydrostatic pressure ( $\Delta p_c$ ) required to induce the complete cyclic MT in this system can be roughly evaluated by a thermodynamic formula:  $\Delta p_c = (A_f - M_f)(dp/dT_0)$  [37]. According to this formula, the values of  $\Delta p_c$  can be estimated to be  $\sim 4.7$  kbar for  $x = 1$ ,  $\sim 5.5$  kbar for  $x = 1.5$ , and  $\sim 6.3$  kbar for  $x = 2$ , which are evidently lower than those reported in Ni-Mn-In [4], Ni-Co-Mn-Sn [6], and Co-Fe-V-Ga [26,27], due to the relatively small  $\Delta T$  and the transforming width. This indicates that a larger and completely reversible BCE, probably used in the cooling machine, would be realized for the studied alloys under a higher hydrostatic pressure.

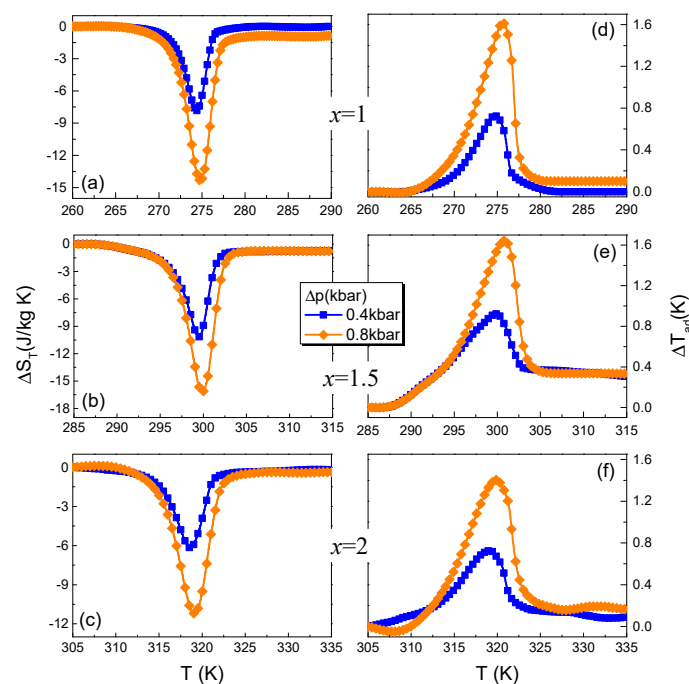


**Figure 5.** (a–c) The isothermal entropy change ( $\Delta S_T$ ), as a function of temperature during the forward MT of  $\text{Co}_{50}\text{V}_{34}\text{Ga}_{16-x}\text{Fe}_x$  for the hydrostatic pressure change of 0.4 kbar and 0.8 kbar. (d–f) The temperature dependence of the adiabatic temperature change ( $\Delta T_{ad}$ ), obtained at same condition.

Figure 6 compare the values of  $\Delta S_T$  and  $\Delta T_{ad}$  for the sample with  $x = 1.5$  to those reported previously in some ferromagnetic, antiferromagnetic, paramagnetic, and ferroelectric barocaloric materials. Under the similar conditions, it is obvious that the barocaloric parameters of  $\text{Co}_{50}\text{V}_{34}\text{Ga}_{14.5}\text{Fe}_{1.5}$  are superior to those obtained in  $\text{BaTiO}_3$  [15], La-Fe-Co-Si [8], Gd-Si-Ge [9],  $\text{PdMnMn}_3$  [38], and a lot of Ni-Mn-based ferromagnetic Heusler alloys [4–6], but they are prominently inferior to some giant barocaloric compounds, including  $\text{Mn}_3\text{GaN}$  [11],  $\text{MnCoGeB}_{0.03}$  [13],  $(\text{MnNiGe})_{0.91}(\text{FeCoGe})_{0.09}$  [14], and the paramagnetic  $\text{Ni}_{50}\text{Mn}_{31.5}\text{Ti}_{18.5}$  [39], whose FOMT can bring about a huge volume change. Despite this fact, our studied alloys have many other advantages, such as a controllable transformation temperature, easy preparation, high mechanical strength, and good oxidation resistance.

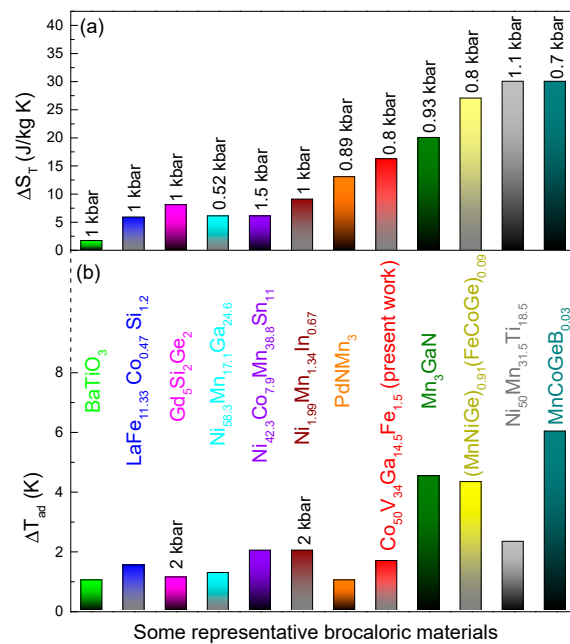


**Figure 6.** (a): The maximum isothermal entropy ( $\Delta S_T$ ) and (b): adiabatic changes ( $\Delta T_{ad}$ ) produced applied a similar hydrostatic pressure for some ferromagnetic, antiferromagnetic, paramagnetic, and ferroelectric barocaloric materials. Data are extracted from [4–6,8,9,11,13–15,34,35].

#### 4. Conclusions

In summary, the influence of Fe substitution for Ga on MT and BCE were systematically studied in  $\text{Co}_{50}\text{V}_{34}\text{Ga}_{16-x}\text{Fe}_x$  ( $1 \leq x \leq 2$ ) alloys. With the increase of the Fe content, the MT significantly moves to a high temperature range, but it is not accompanied by the change of magnetic structure. The hydrostatic pressure-induced MT has been observed in all alloys because they exhibit a visible volume change during the phase transition. Associated with the hydrostatic pressure-induced MT, the optimal barocaloric parameters were obtained in the sample with  $x = 1.5$ , which also performs a better BCE at room temperature when compared with many barocaloric materials previously developed. Although the BCE obtained in the studied alloys is irreversible within the presently applied hydrostatic pressure, a larger and completely reversible effect can be fulfilled under a higher hydrostatic pressure predicted by using the theoretical formular. From our present findings, we can also conclude that the enlargement of the difference in volume between the two phases by manipulating the composition or by using thermal-mechanical training is vital to further optimize the BCE in the Co-V-Ga-based Heusler alloy.

**Author Contributions:** J.L., investigation, methodology, and writing—original draft; Z.L., supervision, project administration, funding acquisition, conceptualization, and writing—review and editing; H.L., formal analysis; L.Y. and Y.Z., methodology; K.X. and Y.C., investigation; Y.L., supervision, project administration, and funding acquisition. All authors have read and agreed to the published version of the manuscript.

**Funding:** This research is funded by the National Nature Science Foundation of China (Project Nos. 51661029 and 51971128), the Program of Shanghai Academic/Technology Research Leader (No. 20XD1401800), and the Innovative Research Team in Science and Technology in the University of Yunnan Province (IRT-STYN).

**Data Availability Statement:** The data presented in this study are available upon request from the corresponding author.

**Acknowledgments:** We express our thanks to Bing Li and Zhao Zhang of the Institute of Metal Research, Chinese Academy of Science, for testing the sample using a  $\mu\text{DSC7}$  EVO and some useful discussions.

**Conflicts of Interest:** The authors declare no conflict of interest.

## References

1. Moya, X.; Kar-Narayan, S.; Mathur, N.D. Caloric materials near ferroic phase transitions. *Nat. Mater.* **2014**, *13*, 439–450. [[CrossRef](#)] [[PubMed](#)]
2. Mañosa, L.; Planes, A. Materials with Giant Mechanocaloric Effects: Cooling by Strength. *Adv. Mater.* **2017**, *29*, 1603607. [[CrossRef](#)]
3. Mañosa, L.; González-Alonso, D.; Planes, A.; Bonnot, E.; Barrio, M.; Tamarit, J.L.; Aksoy, S.; Acet, M. Giant solid-state barocaloric effect in the Ni–Mn–In magnetic shape-memory alloy. *Nat. Mater.* **2010**, *9*, 478–481. [[CrossRef](#)] [[PubMed](#)]
4. Stern-Taulats, E.; Planes, A.; Lloveras, P.; Barrio, M.; Tamarit, J.L.; Pramanick, S.; Majumdar, S.; Yüce, S.; Emre, B.; Frontera, C.; et al. Tailoring barocaloric and magnetocaloric properties in low-hysteresis magnetic shape memory alloys. *Acta Mater.* **2015**, *96*, 324–332. [[CrossRef](#)]
5. He, X.J.; Xu, K.; Wei, S.X.; Zhang, Y.L.; Li, Z.; Jing, C. Barocaloric effect associated with magneto-structural transformation studied by an effectively indirect method for the Ni<sub>58.3</sub>Mn<sub>17.1</sub>Ga<sub>24.6</sub> Heusler alloy. *J. Mater. Sci.* **2017**, *52*, 2915–2923. [[CrossRef](#)]
6. He, X.J.; Kang, Y.R.; Wei, S.X.; Zhang, Y.L.; Cao, Y.M.; Xu, K.; Li, Z.; Jing, C.; Li, Z.B. A large barocaloric effect and its reversible behavior with an enhanced relative volume change for Ni<sub>42.3</sub>Co<sub>7.9</sub>Mn<sub>38.8</sub>Sn<sub>11</sub> Heusler alloy. *J. Alloys Compd.* **2018**, *741*, 821–825. [[CrossRef](#)]
7. Wei, X.Y.; Shen, Y.; Zhang, Z.; Guo, J.P.; Li, B.; Liu, E.K.; Zhang, Z.D.; Liu, J. Low-pressure-induced giant barocaloric effect in an all-*d*-metal Heusler Ni<sub>35.5</sub>Co<sub>14.5</sub>Mn<sub>35</sub>Ti<sub>15</sub> magnetic shape memory alloy. *APL Mater.* **2020**, *8*, 051101. [[CrossRef](#)]
8. Mañosa, L.; González-Alonso, D.; Planes, A.; Barrio, M.; Tamarit, J.L.; Titov, I.S.; Acet, M.; Bhattacharyya, A.; Majumdar, S. Inverse barocaloric effect in the giant magnetocaloric La–Fe–Si–Co compound. *Nat. Commun.* **2011**, *2*, 595. [[CrossRef](#)]
9. Yuce, S.; Barrio, M.; Emre, B.; Stern-Taulats, E.; Planes, A.; Tamarit, J.L.; Mudryk, Y.; Gschneidner, K.A., Jr.; Pecharsky, V.K.; Mañosa, L. Barocaloric effect in the magnetocaloric prototype Gd<sub>5</sub>Si<sub>2</sub>Ge<sub>2</sub>. *Appl. Phys. Lett.* **2012**, *101*, 071906. [[CrossRef](#)]
10. De Oliveira, N.A. Giant magnetocaloric and barocaloric effects in R<sub>5</sub>Si<sub>2</sub>Ge<sub>2</sub> (R = Tb, Gd). *J. Appl. Phys.* **2013**, *113*, 033910. [[CrossRef](#)]
11. Matsunami, D.; Fujita, A.; Takenaka, K.; Kano, M. Giant barocaloric effect enhanced by the frustration of the antiferromagnetic phase in Mn<sub>3</sub>GaN. *Nat. Mater.* **2014**, *14*, 73–78. [[CrossRef](#)] [[PubMed](#)]
12. Wu, R.R.; Bao, L.F.; Hu, F.X.; Wu, H.; Huang, Q.Z.; Wang, J.; Dong, X.L.; Li, G.N.; Sun, J.R.; Shen, F.R.; et al. Giant barocaloric effect in hexagonal Ni<sub>2</sub>In-type Mn–Co–Ge–In compounds around room temperature. *Sci. Rep.* **2015**, *5*, 18027. [[CrossRef](#)] [[PubMed](#)]
13. Aznar, A.; Lloveras, P.; Kim, J.Y.; Stern-Taulats, E.; Barrio, M.; Tamarit, J.L.; Sánchez-Valdés, C.F.; Luis Sánchez Llamazares, J.; Mathur, N.D.; Moya, X. Giant and Reversible Inverse Barocaloric Effects near Room Temperature in Ferromagnetic MnCoGeB<sub>0.03</sub>. *Adv. Mater.* **2019**, *31*, 1903577. [[CrossRef](#)] [[PubMed](#)]
14. Kuang, Y.F.; Qi, J.; Xu, H.J.; Yang, B.; Li, B.; Li, Z.B.; Yan, H.L.; Zhang, Y.D.; Esling, C.; Zhao, X.; et al. Low-pressure-induced large reversible barocaloric effect near room temperature in (MnNiGe)–(FeCoGe) alloys. *Scr. Mater.* **2021**, *200*, 113908. [[CrossRef](#)]
15. Stern-Taulats, E.; Lloveras, P.; Barrio, M.; Defay, E.; Egilmez, M.; Planes, A.; Tamarit, J.L.; Mañosa, L.; Mathur, N.D.; Moya, X. Inverse barocaloric effects in ferroelectric BaTiO<sub>3</sub> ceramics. *APL Mater.* **2016**, *4*, 091102. [[CrossRef](#)]
16. Mikhaleva, E.A.; Flerov, I.N.; Gorev, M.V.; Molokeev, M.S.; Cherepakhin, A.V.; Kartashev, A.V.; Mikhachenok, N.V.; Sablina, K.A. Caloric Characteristics of PbTiO<sub>3</sub> in the Temperature Range of the Ferroelectric Phase Transition. *Phys. Sol. State* **2012**, *54*, 1719. [[CrossRef](#)]
17. Aznar, A.; Lloveras, P.; Romanini, M.; Barrio, M.; Tamarit, J.L.; Cazorla, C.; Errandonea, D.; Mathur, N.D.; Planes, A.; Moya, X.; et al. Giant barocaloric effects over a wide temperature range in superionic conductor AgI. *Nat. Commun.* **2017**, *8*, 1851. [[CrossRef](#)]
18. Bermúdez-García, J.M.; Sánchez-Andújar, M.; Castro-García, S.; López-Beceiro, J.; Artiaga, R.; Señarís-Rodríguez, M.A. Giant barocaloric effect in the ferroic organic-inorganic hybrid [TPrA][Mn(dca)<sub>3</sub>] perovskite under easily accessible pressures. *Nat. Commun.* **2017**, *8*, 15715. [[CrossRef](#)]
19. Li, B.; Kawakita, Y.; Ohira-Kawamura, S.; Sugahara, T.; Wang, H.; Wang, J.F.; Chen, Y.N.; Kawaguchi, S.; Kawaguchi, S.; Ohara, K.; et al. Colossal barocaloric effects in plastic crystals. *Nature* **2019**, *567*, 506–510. [[CrossRef](#)]
20. Lloveras, P.; Aznar, A.; Barrio, M.; Negrier, P.; Popescu, C.; Planes, A.; Mañosa, L.; Stern-Taulats, E.; Avramenko, A.; Mathur, N.D.; et al. Colossal barocaloric effects near room temperature in plastic crystals of neopentylglycol. *Nat. Commun.* **2019**, *10*, 1803. [[CrossRef](#)]
21. Kübler, J.; Fecher, G.H.; Felser, C. Understanding the trend in the Curie temperatures of Co<sub>2</sub>-based Heusler compounds: Ab initio calculations. *Phys. Rev. B* **2007**, *76*, 024414. [[CrossRef](#)]
22. Kanomata, T.; Chieda, Y.; Endo, K.; Okada, H.; Nagasako, M.; Kobayashi, K.; Kainuma, R.; Umetsu, R.Y.; Takahashi, H.; Furutani, Y.; et al. Magnetic properties of the half-metallic Heusler alloys Co<sub>2</sub>VAl and Co<sub>2</sub>VGa under pressure. *Phys. Rev. B* **2010**, *82*, 144415. [[CrossRef](#)]
23. Xu, X.; Nagashima, A.; Nagasako, M.; Omori, T.; Kanomata, T.; Kainuma, R. Martensitic transformation and phase diagram in ternary Co–V–Ga Heusler alloys. *Appl. Phys. Lett.* **2017**, *110*, 121906. [[CrossRef](#)]
24. Liu, C.Q.; Li, Z.; Zhang, Y.L.; Huang, Y.S.L.; Ye, M.F.; Sun, X.D.; Zhang, G.J.; Cao, Y.M.; Xu, K.; Jing, C. Realization of metamagnetic martensitic transformation with multifunctional properties in Co<sub>50</sub>V<sub>34</sub>Ga<sub>16</sub> Heusler alloy. *Appl. Phys. Lett.* **2018**, *112*, 211903. [[CrossRef](#)]

25. Liu, K.; Ma, S.C.; Zhang, Y.X.; Zeng, H.; Yu, G.; Luo, X.H.; Chen, C.C.; Rehman, S.U.; Hu, Y.F.; Zhong, Z.C. Magnetic-field-driven reverse martensitic transformation with multiple magneto-responsive effects by manipulating magnetic ordering in Fe-doped Co-V-Ga Heusler alloys. *J. Mater. Sci. Technol.* **2020**, *58*, 145–154. [[CrossRef](#)]
26. Liu, H.W.; Li, Z.; Zhang, Y.L.; Ni, Z.T.; Xu, K.; Liu, Y.S. A large barocaloric effect associated with paramagnetic martensitic transformation in  $\text{Co}_{50}\text{Fe}_{2.5}\text{V}_{31.5}\text{Ga}_{16}$  quaternary Heusler alloy. *Scr. Mater.* **2020**, *177*, 1–5. [[CrossRef](#)]
27. Liu, K.; Zeng, H.; Qi, J.; Luo, X.H.; Zhao, X.W.; Zheng, X.M.; Yuan, Y.; Chen, C.C.; Ma, S.C.; Xie, R.; et al. Microstructure and giant barocaloric effect induced by low pressure in Heusler  $\text{Co}_{51}\text{Fe}_1\text{V}_{33}\text{Ga}_{15}$  alloy undergoing martensitic transformation. *J. Mater. Sci. Technol.* **2021**, *73*, 76–82. [[CrossRef](#)]
28. Rodriguez-Carvajal, J. Recent advances in magnetic structure determination by neutron powder diffraction. *Physica B* **1993**, *192*, 55–69. [[CrossRef](#)]
29. Khoi, L.D.; Veillet, P.; Campbell, I.A. Hyperfine fields and magnetic interactions in Heusler alloys. *J. Phys. F Met. Phys.* **1978**, *8*, 1811–1825. [[CrossRef](#)]
30. Burch, T.J.; Litrenta, T.; Budnick, J.I. Hyperfine Studies of Site Occupation in Ternary Systems. *Phys. Rev. Lett.* **1974**, *33*, 421–424. [[CrossRef](#)]
31. Ni, Z.T.; Li, Z.; Cao, Y.M.; Liu, H.W.; Zhang, Y.L.; Xu, K.; Liu, Y.S. Influence of hydrostatic pressure on martensitic transformation and strain behavior for  $\text{Co}_{52}\text{V}_{29+x}\text{Ga}_{19-x}$  Heusler alloys. *J. Mater. Sci.* **2021**, *55*, 8317–8324. [[CrossRef](#)]
32. Qian, Y.T.; Wu, M.; Yu, L.T.; Liu, H.W.; Si, X.D.; Luo, X.J.; Li, Z.; Cai, C.B.; Liu, Y.S. Griffiths phase and spontaneous magnetization in polycrystalline  $\text{Co}_{50}\text{V}_{34}\text{Ga}_{16}$  alloy. *J. Alloys Compd.* **2018**, *741*, 821–825. [[CrossRef](#)]
33. Zhang, Y.L.; He, X.J.; Li, Z.; Xu, K.; Liu, C.Q.; Huang, Y.S.; Jing, C. Electrical transport properties and giant baroresistance effect at martensitic transformation of  $\text{Ni}_{43.7}\text{Fe}_{5.3}\text{Mn}_{35.4}\text{In}_{15.6}$  Heusler alloy. *Appl. Phys. Lett.* **2018**, *112*, 182402. [[CrossRef](#)]
34. Pecharsky, V.K.; Gschneidner, K.A. Giant Magnetocaloric Effect in  $\text{Gd}_5(\text{Si}_2\text{Ge}_2)$ . *Phys. Rev. Lett.* **1997**, *78*, 4494–4497. [[CrossRef](#)]
35. Wade, H.; Tanabe, Y. Giant magnetocaloric effect of  $\text{MnAs}_{1-x}\text{Sb}_x$ . *Appl. Phys. Lett.* **2001**, *79*, 3302–3304. [[CrossRef](#)]
36. Tegus, O.; Brück, E.; Buschow, K.H.J.; de Boer, F.R. Transition-metal-based magnetic refrigerants for room-temperature applications. *Nature* **2002**, *415*, 150–152. [[CrossRef](#)]
37. Shamberger, P.J.; Ohuchi, F.S. Hysteresis of the martensitic phase transition in magnetocaloric effect Ni-Mn-Sn alloys. *Phys. Rev. B* **2009**, *79*, 144407. [[CrossRef](#)]
38. Tao, K.; Song, W.H.; Lin, J.C.; Zhang, X.K.; Tong, P.; Zhang, Z.; Qi, J.; Li, B.; Ling, L.S.; Ma, L.; et al. Giant reversible barocaloric effect with low hysteresis in antiperovskite  $\text{PdNMn}_3$  compound. *Scr. Mater.* **2021**, *203*, 114049. [[CrossRef](#)]
39. Aznar, A.; Gràcia-Condal, A.; Planes, A.; Lloveras, P.; Barrio, M.; Tamarit, J.L.; Xiong, W.X.; Cong, D.Y.; Popescu, C.; Mañosa, L. Giant barocaloric effect in all-d-metal Heusler shape memory alloys. *Phys. Rev. Mater.* **2019**, *3*, 044406. [[CrossRef](#)]